

H α as a tracer of star formation in the SPHINX cosmological simulations

I. G. Kramarenko^{1,*}, J. Rosdahl², J. Blaizot², J. Matthee¹, H. Katz^{3,4} and C. Di Cesare¹

¹ Institute of Science and Technology Austria (ISTA), Am Campus 1, 3400 Klosterneuburg, Austria

² Univ Lyon, Univ Lyon1, Ens de Lyon, CNRS, Centre de Recherche Astrophysique de Lyon UMR5574, F-69230, Saint-Genis-Laval, France

³ Department of Astronomy & Astrophysics, University of Chicago, 5640 S Ellis Avenue, Chicago, IL 60637, USA

⁴ Kavli Institute for Cosmological Physics, University of Chicago, Chicago IL 60637, USA

Received XXX; accepted YYY

ABSTRACT

The H α emission line in galaxies is a powerful tracer of their recent star formation activity. With the advent of *JWST*, we are now able to routinely observe H α in galaxies at high redshift ($z \gtrsim 3$) and thus measure their star formation rates (SFRs). However, using classical SFR(H α) calibrations to derive the SFRs leads to biased results because high-redshift galaxies are commonly characterized by low metallicities and bursty star formation histories, affecting the conversion factor between the H α luminosity ($L_{\text{H}\alpha}$) and the SFR. In this work, we develop a set of new SFR(H α) calibrations that allow us to predict the SFRs of H α -emitters at $z \gtrsim 3$ with minimal error. We use the SPHINX cosmological simulations to select a sample of star-forming galaxies representative of the H α -emitter population observed with *JWST*. We then derive linear corrections to the classical SFR(H α) calibrations, taking into account variations in the physical properties (e.g., stellar metallicities) among individual galaxies. We obtain two new SFR(H α) calibrations that, compared to the classical calibrations, reduce the root mean squared error (RMSE) in the predicted SFRs by $\Delta\text{RMSE} \approx 0.04$ dex and $\Delta\text{RMSE} \approx 0.06$ dex, respectively. Using the recent *JWST* NIRCcam/grism observations of H α -emitters at $z \sim 6$, we show that the new calibrations affect the high-redshift galaxy population statistics: (i) the estimated cosmic star formation rate density decreases by $\Delta\rho_{\text{SFR}} \approx 12\%$, and (ii) the observed slope of the star formation main sequence increases by $\Delta\partial \log \text{SFR} / \partial \log M_{\star} = 0.08 \pm 0.02$.

Key words. galaxies: fundamental parameters – galaxies: evolution – galaxies: formation – galaxies: high-redshift – galaxies: star formation

1. Introduction

One of the most fundamental and basic properties of galaxies is the rate at which new stars form, the star formation rate (SFR). The SFR is sensitive to the interplay between the gas inflow and outflow rates of galaxies, and the efficiency at which this gas is converted into stars (e.g., Bouché et al. 2010; Lilly et al. 2013; Behroozi et al. 2019). The SFR can fluctuate on different timescales (e.g., Sparre et al. 2015; Iyer et al. 2020; Flores Velázquez et al. 2021), which range from dynamical timescales of molecular clouds (~ 10 s of Myrs), through galaxy merger timescales (~ 100 Myr), to long (Gyr-scale) coherences in accretion rates (e.g., Matthee & Schaye 2019; Wang & Lilly 2020; Tacchella et al. 2020; Wan et al. 2025). Observationally, SFRs can be measured using various diagnostics (e.g., Kennicutt & Evans 2012; De Looze et al. 2014; Davies et al. 2019) that are either based on the light from massive, short-lived stars (e.g., the rest-frame UV), or processed radiation (e.g., nebular lines in HII regions or dust emission). Each of these diagnostics probes different timescales of star formation and is affected by dust attenuation differently.

At high redshifts ($z > 3$), the rest-frame UV emission used to be the most sensitive SFR indicator that could be measured for large galaxy samples, tracing star formation on $t \sim 100$ Myr timescales (e.g., Bouwens et al. 2015). However, dust corrections in the rest-frame UV are significant, with potentially up to

50% of the cosmic star formation rate density (ρ_{SFR}) at $z \sim 5$ being obscured by dust (e.g., Zavala et al. 2021; Sun et al. 2025). This emphasizes the great importance of alternative SFR indicators that are less sensitive to dust attenuation, such as the H α emission. The H α photons are emitted in the rest-frame optical ($\lambda = 6564 \text{ \AA}$), where dust corrections are smaller than in the rest-frame UV due to the negative slope of the dust attenuation curve (however, we caution that there is growing evidence of flatter attenuation curves at fixed A_V or stellar mass at high redshifts compared to the local Universe; e.g., Shivaei et al. 2025; Fisher et al. 2025). The luminosity of the H α line is directly proportional to the luminosity of ionizing photons that are predominantly emitted by very young stellar populations, making H α sensitive to star formation on shorter timescales ($t \sim 10$ Myr; e.g., Leitherer et al. 1999). As the *JWST* can now measure the distribution of H α luminosities out to $z \sim 7$ based on spectroscopy and narrow-band imaging (e.g., Clarke et al. 2024; Pirie et al. 2025; Covello-Paz et al. 2025; Fu et al. 2025), it is timely to reassess the role of the H α emission as a tracer of the SFR.

The conversion factor between the H α luminosity¹ and the SFR primarily depends on assumptions on the properties of stellar populations, in particular, the star formation history (SFH), the initial mass function (IMF), binarity, and stellar metallicity (e.g., Wilkins et al. 2019). The SFH and IMF are relevant because the ionizing photon emissivity from a single stellar popu-

¹ Throughout this work, we assume a negligible contribution of active galactic nuclei to the H α emission.

* email: ivan.kramarenko@ista.ac.at

lation drops sharply after a few Myr when massive, short-lived O stars leave the main sequence. Binary interactions can extend these ionizing lifetimes (Götberg et al. 2017), smoothing the otherwise steep drop-off after a few Myrs. At fixed stellar mass and age, the metallicity affects the effective temperature of stellar atmospheres due to line blanketing effects, affecting the ionizing luminosity as well.

The classical SFR($H\alpha$) calibration proposed by Kennicutt (1998) (see also Kennicutt & Evans 2012) assumes a constant SFH over $t = 100$ Myr and solar metallicity, based on the typical conditions in galaxies in the low-redshift Universe. However, various spectroscopic observations of galaxies at high redshifts suggest that their SFHs are bursty (e.g., Asada et al. 2024; Endsley et al. 2024; Cole et al. 2025; Carvajal-Bohorquez et al. 2025). Further, given the gas-phase oxygen abundances are typically measured to be $\sim 10\%$ solar (Curti et al. 2024; Scholte et al. 2025), and early galaxies are expected to be α -enhanced due to the rapid formation timescales (e.g., Chruślińska et al. 2024), the iron-peak element abundances are likely to be low. This implies hotter stars and a more efficient $H\alpha$ photon production at a fixed SFR (e.g., Theios et al. 2019) than at low redshift.

The aim of this paper is to revisit the classical SFR($H\alpha$) calibrations to predict the SFRs of galaxies at high redshift ($z \gtrsim 3$). Instead of using idealistic models with constant SFHs and fixed stellar metallicities, we use simulated galaxies and their modeled $H\alpha$ luminosities from the SPHINX cosmological radiation-hydrodynamical simulation (Rosdahl et al. 2018; Katz et al. 2023). These cosmological simulations self-consistently model SFHs and metal enrichment processes and are calibrated to match various observables at high redshifts ($z \sim 6$). The simulated volume matches the typical volumes of deep JWST surveys well, which enables a high resolution that can capture SFR variations on short timescales ($t \sim 1$ Myr) and approximate the distribution of gas in the interstellar medium relevant for radiative transfer effects.

In Sect. 2, we briefly describe the SPHINX simulations and explain how the $H\alpha$ luminosities are derived. In Sect. 3, we present a set of simulation-inferred SFR($H\alpha$) calibrations that predict the SFRs of SPHINX galaxies with minimal error. Finally, we discuss the implications of our work in Sect. 4 and summarize in Sect. 5.

2. Methods

In this work, we use the simulated galaxy data from SPHINX, a suite of cosmological radiation-hydrodynamic simulations (Rosdahl et al. 2018). SPHINX leverages the adaptive mesh refinement code RAMSES-RT (Rosdahl et al. 2013; Teyssier 2002) to simulate tens of thousands of galaxies in the epoch of reionization. The ISM is resolved down to 76 co-moving pc, corresponding to a physical resolution of 11 pc at $z = 6$. The dark matter halos are resolved down to the atomic cooling threshold ($M_{\text{vir}} \approx 3 \times 10^7 M_{\odot}$). Hydrodynamics, non-equilibrium thermochemistry, and radiative transfer of Lyman-continuum radiation (LyC; $\lambda < 912\text{\AA}$) are performed self-consistently on the fly, with subgrid implementations for gas cooling, star formation, metal enrichment, and feedback. The on-the-fly radiative emission and propagation of LyC photons make SPHINX an excellent model for accurately predicting how $H\alpha$ emission traces star formation in the simulated galaxies.

Our analysis is based on the data from the SPHINX²⁰ Public Data Release, Version 1 (SPDRv1; Katz et al. 2023). SPHINX²⁰ is the largest simulation of the SPHINX suite, with a periodic box with volume of $(20 \text{ cMpc})^3$ simulated down to a redshift of

$z = 4.64$ (Rosdahl et al. 2022). SPHINX²⁰ uses the BPASSv2.2 stellar population synthesis (SPS) model (Stanway & Eldridge 2018), which adopts a Kroupa (2001) IMF with an upper mass cutoff of $100 M_{\odot}$ and a slope of -1.3 from 0.1 to $0.5 M_{\odot}$ and -2.35 from 0.5 to $100 M_{\odot}$. The intrinsic Balmer line luminosities are generated by interpolating the CLOUDY v17.03 models (Ferland et al. 2017) for gas cells that host stellar particles with unresolved Stromgren spheres, or by using the non-equilibrium ionizing fractions from the simulation otherwise. For each halo, the total intrinsic line emission is then the sum of the line luminosities of all gas cells within the virial radius of the halo. The equivalent widths are calculated by taking the stellar and nebular continuum emission into account, generated as detailed in Katz et al. (2023).

We post-process the line and continuum radiation, subject to absorption and scattering by dust, using the radiative transfer code RASCAS (Michel-Dansac et al. 2020). Dust is assigned to the gas cells using the Small Magellanic Cloud (SMC) dust model from Laursen et al. (2009). We note that the dust attenuation curve at high redshifts likely has a steeper slope than the SMC slope (e.g., Shivaei et al. 2025; Markov et al. 2025), possibly due to changes in the dust grain properties. Next, 200,000 photon packets are probabilistically distributed to the gas cells, with the initial wavelengths placed at the line centers, thermally broadened, and shifted according to the bulk velocity of the cell. Likewise, 200,000 photon packets are probabilistically distributed to the star particles (gas cells) based on the luminosities of the stellar (nebular) continuum at the line centers. The observed line luminosities and equivalent widths are then obtained by computing the escape fractions of each component (for details, see Katz et al. 2023).

Due to the computation time and data storage limitations, SPDRv1 only includes SPHINX²⁰ galaxies with $\text{SFR}_{10} \geq 0.3 M_{\odot} \text{ yr}^{-1}$, where SFR_{10} is the SFR averaged over $t = 10$ Myr. This excludes objects that are likely too faint to be observed with JWST (Katz et al. 2023), unless lensing is considered (e.g., Bezanson et al. 2024; Naidu et al. 2024). However, an SFR cut also leads to an incompleteness in the SFR— $L_{H\alpha}$ relation at low luminosities, which can bias our results. We therefore limit our selection of galaxies from SPDRv1 to those with an observed $H\alpha$ luminosity ($L_{H\alpha}^{\text{obs}}$) greater than $L_{H\alpha}^{\text{obs}} = 1.8 \times 10^{41} \text{ erg s}^{-1}$ (here, we use the simulation-based luminosities calculated as described above). This value is motivated by the recent $H\alpha$ LF measurements from JWST NIRCcam/grism, which reach similar luminosities at the faint end (e.g., Fu et al. 2025). Crucially, this selection yields a complete $H\alpha$ -emitter sample, which we check by running RASCAS on all SPHINX²⁰ halos whose intrinsic $H\alpha$ luminosity ($L_{H\alpha}^{\text{int}}$) exceeds the luminosity cut. We also try $L_{H\alpha}^{\text{obs}} > 1.0 \times 10^{41} \text{ erg s}^{-1}$ and $L_{H\alpha}^{\text{obs}} > 3.0 \times 10^{41} \text{ erg s}^{-1}$ cuts, finding little impact on our results. With this additional luminosity cut, our final sample comprises $N = 63, 66, 48, 36, 22, 17,$ and 13 galaxies at $z = 4.64, 5, 6, 7, 8, 9,$ and 10 , respectively, with a total of $N = 265$ galaxies.

The SN feedback model in SPHINX is calibrated to match the UV luminosity function (UVLF) at $z = 6$ (see App. C in Rosdahl et al. 2018). A possible caveat is that the stellar mass-halo mass relation in SPHINX is 0.5 – 1.0 dex higher than predicted by the Behroozi et al. (2019) model, for example, which matches a broad array of observational data, including stellar mass functions at $z = 0$ – 4 and median UV—stellar mass relations at $z = 4$ – 8 (see Fig. 4 in Katz et al. 2023). Furthermore, the stellar mass function (SMF) in SPHINX is significantly overestimated compared to the SMF inferred from the JWST/NIRCcam observations at $z = 5$ – 6 (Weibel et al. 2024). If the stellar masses

of SPHINX galaxies are overestimated, the SFRs should also be overestimated on average. This implies that the amount of dust in the simulation should be higher than in the real Universe in order to match the UVLF. The excess of dust would then explain the fact that SPHINX predicts lower $H\alpha$ and $[O\text{III}]$ luminosities at fixed stellar mass than those measured by *JWST* (e.g., Covelopaz et al. 2025; Meyer et al. 2024). Although the possibility of SPHINX galaxies having too much dust does not affect our main results as they are based on the intrinsic $H\alpha$ properties (Sect. 3), it will become important later for understanding the errors in the $\text{SFR}(H\alpha)$ calibrations that use the observed $H\alpha$ (Sect. 4).

3. Results

In this section, we investigate the intrinsic (i.e., without taking dust attenuation into account) $\text{SFR}-L_{H\alpha}$ relation in the SPHINX²⁰ cosmological simulation. We compare this relation to the $\text{SFR}(H\alpha)$ calibrations from the literature and study the effect of the variations in the physical properties of individual galaxies (metallicity, stellar age, etc.) on the accuracy of the predicted SFRs. Based on this analysis, we develop a set of new $\text{SFR}(H\alpha)$ calibrations that minimize the error in $H\alpha$ -derived SFRs at high redshift.

Unless otherwise specified, we use the SFRs averaged over the last $t = 10$ Myr of the SFH. This choice is motivated by the fact that nebular emission lines such as $H\alpha$ trace stars with lifetimes of $t \sim 3-10$ Myr (e.g., Kennicutt & Evans 2012). This is further supported by the simulation itself, where the correlation coefficient between the SFR and $L_{H\alpha}^{\text{int}}$ peaks between $4 \text{ Myr} \lesssim t \lesssim 12 \text{ Myr}$ ($r \approx 0.95-0.98$; see Sect. A).

3.1. The $\text{SFR}-L_{H\alpha}$ relation in SPHINX

Figure 1 shows the intrinsic $\text{SFR}-L_{H\alpha}$ relation for the galaxy sample selected from the SPHINX²⁰ simulation as described in Sect. 2. In the same figure, we show different $\text{SFR}(H\alpha)$ calibrations proposed in the literature. These include the original K98 calibration ($C_{H\alpha} = -41.1$), the K98 calibration converted to the Kroupa IMF (Kroupa 2001; $C_{H\alpha} = -41.3$), and two calibrations from Theios et al. (2019, hereafter T19) calculated for a Kroupa-type IMF and solar metallicity ($C_{H\alpha} = -41.35$), and the same IMF but subsolar metallicity ($Z_* = 0.1Z_\odot$; $C_{H\alpha} = -41.64$), respectively. Here, $C_{H\alpha}$ is the conversion factor between $L_{H\alpha}^{\text{int}}$ and SFR, defined as follows:

$$\log_{10} \left[\frac{\text{SFR}}{M_\odot \text{ yr}^{-1}} \right] = \log_{10} \left[\frac{L_{H\alpha}^{\text{int}}}{\text{erg s}^{-1}} \right] + C_{H\alpha}. \quad (1)$$

Figure 1 reveals that a constant $C_{H\alpha}$ cannot provide an accurate estimate of the SFRs of SPHINX galaxies across the full $L_{H\alpha}^{\text{int}}$ range. Specifically, the T19 calibration that assumes $Z_* = Z_\odot$ (the dashed blue line in Fig. 1) matches the median $\text{SFR}-L_{H\alpha}$ relation in SPHINX at high luminosities well ($\log_{10}(L_{H\alpha}^{\text{int}}/\text{erg s}^{-1}) \gtrsim 42.2$). In contrast, the same $\text{SFR}(H\alpha)$ calibration at low luminosities ($\log_{10}(L_{H\alpha}^{\text{int}}/\text{erg s}^{-1}) \lesssim 42.2$) overestimates the SFRs by $\approx 0.1-0.2$ dex. Decreasing $C_{H\alpha}$ would result in a better match at low luminosities, but the SFRs at high luminosities would then be underestimated.

We note that the median $\text{SFR}-L_{H\alpha}$ relation in SPHINX at low luminosities lies between the two T19 calibrations that differ only in the assumption on metallicity ($Z_* = 0.1Z_\odot$ vs. $Z_* = Z_\odot$; indicated by the solid and dashed blue lines in Fig. 1, respectively). Motivated by this result, we test whether the variations

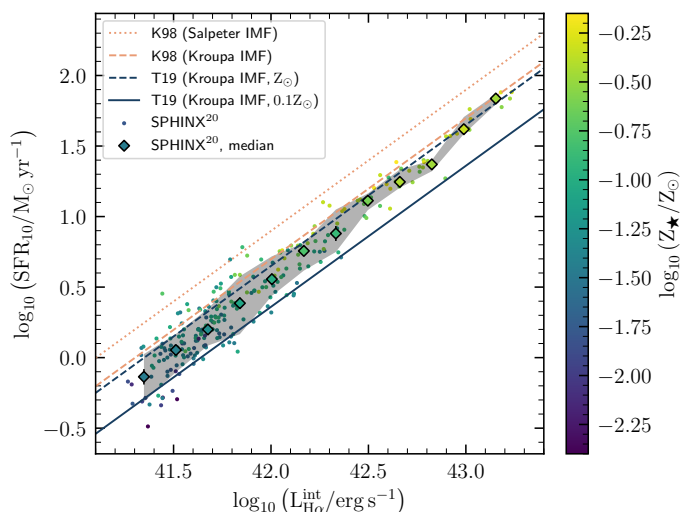


Fig. 1. Intrinsic $\text{SFR}-L_{H\alpha}$ relation in the SPHINX²⁰ cosmological simulation, color-coded by the stellar metallicity. The SFR values are averaged over $t = 10$ Myr, i.e., the typical lifetime of stars traced by $H\alpha$. The diamonds show the median SFR in the bins of $L_{H\alpha}^{\text{int}}$, with the error bars showing the standard error on the median. The shaded region indicates the 68% (1σ) confidence interval. The diagonal lines show the $\text{SFR}(H\alpha)$ calibrations from the literature, i.e. (top to bottom): the original K98 calibration, the K98 calibration converted to the Kroupa IMF, and two calibrations from T19 calculated for the Kroupa IMF and two different metallicities ($Z_* = Z_\odot$ and $Z_* = 0.1Z_\odot$, respectively).

in metallicity might be a key factor driving the evolution of the median $\text{SFR}-L_{H\alpha}$ relation in SPHINX. We split our sample into low- and high- $L_{H\alpha}^{\text{int}}$ groups ($\log_{10}(L_{H\alpha}^{\text{int}}/\text{erg s}^{-1}) < 42.2$ and $\log_{10}(L_{H\alpha}^{\text{int}}/\text{erg s}^{-1}) > 42.2$, respectively), and calculate the median stellar metallicity² in each group. We obtain $Z_* = 0.06Z_\odot$ and $Z_* = 0.33Z_\odot$ in the low- and high- $L_{H\alpha}^{\text{int}}$ groups, respectively. In other words, brighter galaxies are more metal-rich on average, which reflects the mass-metallicity relation (MZR) in SPHINX (for a discussion, see Katz et al. 2023), and likely causes an upturn of the median $\text{SFR}-L_{H\alpha}$ relation at high luminosities (see also Fig. 1, where the markers are color-coded by metallicity).

Figure 1 further demonstrates that the original K98 calibration (indicated by the dotted orange line) overestimates the SFRs by $\approx 0.3-0.5$ dex compared to SPHINX. One of the main reasons for this discrepancy is the difference in the IMFs: K98 uses the Salpeter (1955) IMF, whereas SPHINX uses a Kroupa-type IMF. After rescaling to the Kroupa IMF, the K98 calibration still predicts $\approx 0.1-0.3$ dex higher SFRs than the simulation (the dashed orange line in Fig. 1). This difference cannot be eliminated even when using the T19 calibration which, unlike the K98 calibration, assumes the same stellar population synthesis model as SPHINX (i.e., BPASSv2.2; the dashed blue line in Fig. 1). Therefore, the only way to fully reconcile the K98 calibration and the simulation data is to assume a sub-solar metallicity, for some galaxies as low as $Z_* = 0.1Z_\odot$ (the solid blue line in Fig. 1). As discussed in the introduction, a subsolar metallicity like this agrees well with the current estimates of the gas-phase metallicity and also with the direct estimates of stellar metallicities of galaxies at $z \sim 2-3$ (Steidel et al. 2016; Cullen et al. 2019), although we caution that these were derived assuming constant SFHs, which might impact the results (Matthee et al. 2022).

² Hereafter, stellar metallicities (and ages) of SPHINX galaxies are weighted by the LyC luminosity.

Figure 1 also reveals that the SFR— $L_{H\alpha}$ relation in SPHINX exhibits significant scatter around the median relation (hereafter, σ_{SFR}). In particular, we find that σ_{SFR} decreases from $\sigma_{\text{SFR}} \approx 0.17$ dex at $\log_{10}(L_{H\alpha}^{\text{int}}/\text{erg s}^{-1}) = 41.3$ to $\sigma_{\text{SFR}} \approx 0.04$ dex at $\log_{10}(L_{H\alpha}^{\text{int}}/\text{erg s}^{-1}) = 42.8$, and has a median $\sigma_{\text{SFR}} = 0.11$ dex. This scatter is neglected by the existing SFR($H\alpha$) calibrations, leading to errors in the predicted SFRs of individual galaxies. To quantify this effect, we introduce the SFR bias factor, defined as the ratio of the SFR predicted from $H\alpha$ to the true SFR directly tracked by the simulation: $\Delta_{\text{SFR}} \equiv \text{SFR}(H\alpha)/\text{SFR}_{10}$. Here, we use the T19 calibration that assumes $Z_* = Z_{\odot}$ to calculate SFR($H\alpha$) as this calibration provides the best match to the SPHINX data (see Fig. 1). We note that using a different calibration would only change Δ_{SFR} by a constant factor (in logarithmic scale) without affecting any trends observed between Δ_{SFR} and the physical properties of SPHINX galaxies.

We find that Δ_{SFR} decreases with stellar metallicity ($r = -0.51$, $p < 10^{-6}$; Fig. 2, top panel), in agreement with our earlier analysis of the median SFR— $L_{H\alpha}$ relation in SPHINX. However, we also report a significant scatter in Δ_{SFR} at fixed Z_* : $\sigma \approx 0.09$ dex. This indicates that metallicity alone does not cause the variations in the SFRs of SPHINX galaxies with respect to the SFRs predicted from $H\alpha$. In particular, we find that Δ_{SFR} shows a negative correlation with stellar age ($r = -0.59$, $p < 10^{-6}$; Fig. 2, bottom panel), with an average scatter of $\sigma \approx 0.07$ dex. Notably, galaxies with young stellar populations ($t_{\text{age}} \lesssim 5$ Myr) exhibit high Δ_{SFR} (≈ 0.1 – 0.4 dex). Even if we use the best-fit SFR($H\alpha$) calibration in the form of Eq. (1) ($C_{H\alpha} = -41.45$), Δ_{SFR} still reaches ≈ 0.3 dex at $t_{\text{age}} \approx 2$ – 3 Myr. This bias can be explained by the fact that the existing SFR($H\alpha$) calibrations assume constant star formation over a long timescale (typically $t = 100$ Myr or $t = 1$ Gyr; e.g., Hao et al. 2011). This assumption breaks down in the simulation, where galaxies exhibit very bursty and stochastic SFHs (Katz et al. 2023).

We also examine the relationship between Δ_{SFR} and stellar mass and find a negative correlation ($r = -0.44$, $p < 10^{-6}$), likely driven by the positive scaling of stellar mass with metallicity (see Katz et al. 2023 for the discussion of the MZR in SPHINX). Finally, we check the dependence of Δ_{SFR} on the escape fraction of ionizing radiation (f_{esc}) and find a nearly flat trend ($r = -0.21$, $p = 0.0009$). This result is expected because the strength of nebular emission lines is inversely proportional to the escape fraction of ionizing photons, $\propto (1 - f_{\text{esc}})$, and SPHINX galaxies have low f_{esc} ($f_{\text{esc}} \lesssim 1\%$) on average. This agrees with high-redshift observations, where f_{esc} is also estimated to be low ($< 10\%$; e.g., Mascia et al. 2024).

3.2. Simulation-informed SFR($H\alpha$) calibrations

Using the insights gained from our analysis of the SFR— $L_{H\alpha}$ relation in SPHINX, we discuss possible improvements to the existing SFR($H\alpha$) calibrations that take the form of Eq. (1). For example, stellar metallicity could be a useful parameter to include in the calibration to reduce the error in the predicted SFR (see Fig. 2). However, measuring stellar metallicity is difficult in practice, and we therefore only use quantities that can be measured robustly from galaxy spectra. Specifically, we run an ordinary least-squares (OLS) model similar to Eq. (1), but allowing the $\log_{10}(L_{H\alpha}^{\text{int}}/\text{erg s}^{-1})$ coefficient to vary. We use the randomly selected 80% of the sample to train the model and the remaining 20% to validate its performance. The resulting SFR($H\alpha$) calibra-

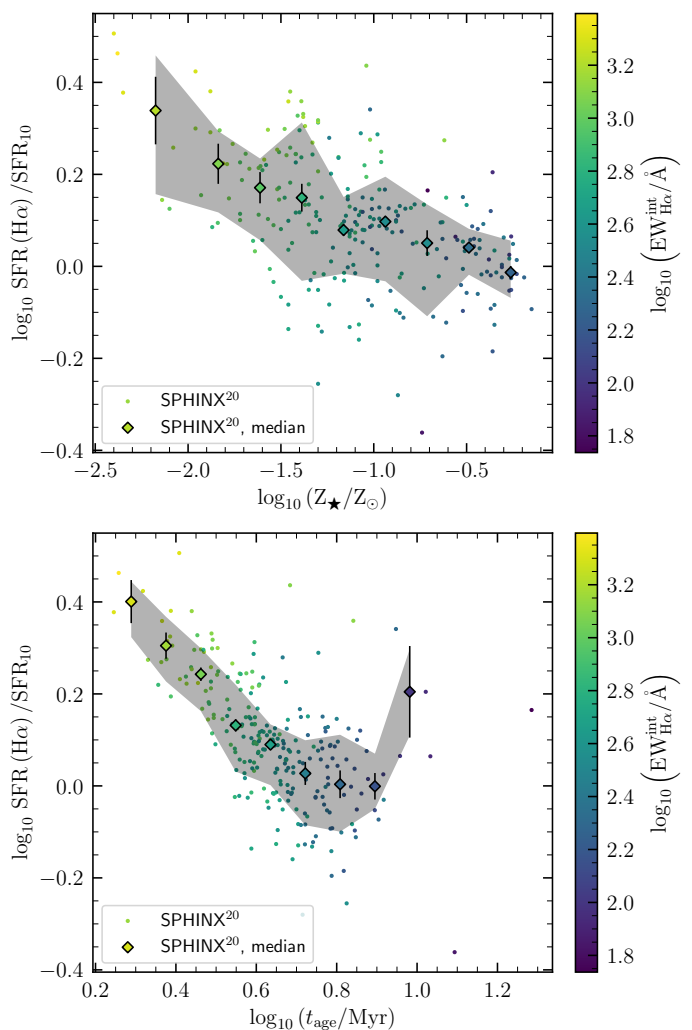


Fig. 2. SFR bias factor ($\Delta_{\text{SFR}} \equiv \text{SFR}(H\alpha)/\text{SFR}_{10}$) as a function of stellar metallicity (top) and age (bottom) in SPHINX, color-coded by $\text{EW}_{H\alpha}$. The SFR($H\alpha$) values are calculated using the T19 calibration ($Z_* = Z_{\odot}$). The diamonds show the running median, with the error bars indicating the standard error on the median. The shaded region indicates the 68% (1σ) confidence interval.

tion can be written as follows:

$$\log_{10} \left[\frac{\text{SFR}}{M_{\odot} \text{ yr}^{-1}} \right] = \log_{10} \left[\frac{L_{H\alpha}^{\text{int}}}{\text{erg s}^{-1}} \right] - 41.45 + 0.06 \left(\log_{10} \left[\frac{L_{H\alpha}^{\text{int}}}{\text{erg s}^{-1}} \right] - 41.90 \right), \quad (2)$$

where the last term is the effective correction to Eq. (1). The root mean squared error (RMSE) calculated on the training and test datasets is identical (RMSE = 0.13 dex), indicating that the model performs well on unseen data. Compared to the T19 calibration ($Z_* = Z_{\odot}$) which yields RMSE = 0.17 dex calculated on the full dataset, the RMSE is reduced by ≈ 0.04 dex (see also Fig. 3).

The SFR($H\alpha$) calibration given in Eq. (2) corrects the SFRs by a factor that depends on $L_{H\alpha}$ alone, which means that σ_{SFR} is neglected even when using the updated calibration. To further improve on this, we add a correction to Eq. (2) that depends on the $H\alpha$ equivalent width ($\text{EW}_{H\alpha}$). This choice is motivated by the fact that $\text{EW}_{H\alpha}$ traces stellar metallicity and age, which both drive σ_{SFR} (Fig. 2). In addition, $\text{EW}_{H\alpha}$ is only weakly sensitive

to dust attenuation, which implies that dust corrections affect the results less than when other observables are used (e.g., M_{UV}). We therefore run an OLS model that includes $EW_{H\alpha}$, using the same training sample as in Eq. (2). The resulting SFR($H\alpha$) calibration can be written as follows:

$$\begin{aligned} \log_{10} \left[\frac{\text{SFR}}{M_{\odot} \text{ yr}^{-1}} \right] &= \log_{10} \left[\frac{L_{H\alpha}^{\text{int}}}{\text{erg s}^{-1}} \right] - 41.45 \\ &- 0.01 \left(\log_{10} \left[\frac{L_{H\alpha}^{\text{int}}}{\text{erg s}^{-1}} \right] - 41.90 \right) \\ &- 0.26 \left(\log_{10} \left[\frac{EW_{H\alpha}^{\text{int}}}{\text{\AA}} \right] - 2.67 \right), \end{aligned} \quad (3)$$

where the last two terms are the effective corrections to Eq. (1). The new calibration yields $\text{RMSE} = 0.11$ dex on the training and test datasets, which is ≈ 0.02 dex lower than the RMSE calculated using Eq. (2), or ≈ 0.06 dex lower than the RMSE calculated using the T19 calibration ($Z_* = Z_{\odot}$). Figure 3 compares these calibrations as a function of $L_{H\alpha}^{\text{int}}$. In particular, this plot shows that the median Δ_{SFR} in the $L_{H\alpha}^{\text{int}}$ bins is within ± 0.05 dex across the entire range of luminosities ($41.25 < \log_{10}(L_{H\alpha}^{\text{int}}/\text{erg s}^{-1}) < 43.25$) when using Eq. (2) or Eq. (3). This is an improvement over the T19 calibration, which overpredicts the SFRs by $\Delta_{\text{SFR}} \gtrsim 0.1$ dex in galaxies with low to medium luminosities ($41.25 < \log_{10}(L_{H\alpha}^{\text{int}}/\text{erg s}^{-1}) \lesssim 42.5$). The standard deviation of Δ_{SFR} in the $L_{H\alpha}^{\text{int}}$ bins (hereafter $\sigma_{\Delta_{\text{SFR}}}$) is nearly identical between the T19 calibration and the SFR($H\alpha$) calibration given in Eq. (2) ($\sigma_{\Delta_{\text{SFR}}} \approx 0.11$ dex), but it decreases by ≈ 0.03 dex ($\sigma_{\Delta_{\text{SFR}}} \approx 0.08$ dex) for Eq. (3), especially at medium luminosities ($41.8 \lesssim \log_{10}(L_{H\alpha}^{\text{int}}/\text{erg s}^{-1}) \lesssim 42.5$).

We also run a similar model in which we replace $EW_{H\alpha}$ with $[\text{O III}]/H\beta$, which is a proxy for the gas-phase (and, to a weaker extent, stellar) metallicity. The resulting calibration shows the same performance as Eq. (3) ($\text{RMSE} = 0.11$ dex). Given the broader wavelength coverage required to measure $[\text{O III}]/H\beta$ compared to $EW_{H\alpha}$, we find Eq. (3) to be more practical when applied to observations and hence use it as our best-performance calibration for the remainder of this paper.

4. Discussion

4.1. Implications

The $H\alpha$ line has long been known as a reliable indicator of the SFR as it traces the ionizing photon luminosity from massive ($M > 10M_{\odot}$), short-lived ($t \lesssim 10$ Myr) stars (e.g., Kennicutt 1998). Over the past decades, $H\alpha$ has been widely employed in numerous spectroscopic (e.g., Shim et al. 2009; Gunawardhana et al. 2013; Nagaraj et al. 2023) and narrow-band imaging (e.g., Ly et al. 2007; Hayes et al. 2010; Sobral et al. 2013) surveys to measure the cosmic SFH up to $z \sim 3$. With the recent advent of sensitive near-IR spectroscopy at $\lambda \sim 3\text{--}5 \mu\text{m}$, these measurements have been extended to $z \approx 3\text{--}6$, in particular thanks to the *JWST*/NIRCam slitless spectroscopic observations of large samples of $H\alpha$ -emitters at the same redshifts (e.g., Covelo-Paz et al. 2025; Fu et al. 2025; Lin et al. 2026).

As $H\alpha$ observations become more accessible at high redshift, it is crucial to revisit the classical SFR($H\alpha$) calibrations (e.g., Kennicutt 1998) that are commonly used at $z \lesssim 3$. Based on a realistic galaxy simulation, we have shown that these calibrations bias the predicted SFRs under the physical conditions that are characteristic of high-redshift galaxies observed with *JWST*

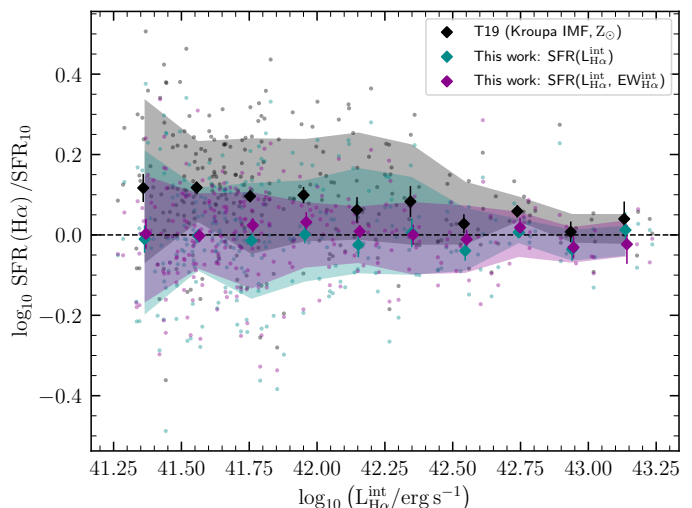


Fig. 3. Comparison of the SFR($H\alpha$) calibrations as a function of the intrinsic $H\alpha$ luminosity: T19 calibration (gray) and the new SFR($H\alpha$) calibrations given in Eq. (2) (cyan) and Eq. (3) (magenta). The vertical axis represents the SFR bias factor ($\Delta_{\text{SFR}} \equiv \text{SFR}(H\alpha) / \text{SFR}_{10}$; closer to $\log \Delta_{\text{SFR}} = 0$ is better). The diamonds show the running median, with the error bars indicating the standard error on the median. The shaded regions indicate the 68% (1σ) confidence interval.

(i.e., a low metallicity and bursty star formation), potentially also affecting population statistics. To quantify this effect, we study the effect of the metallicity- and age-dependent SFR bias (see Fig. 2) on the ρ_{SFR} measurements. Specifically, we convert the dust-corrected $H\alpha$ luminosity function at $z \sim 6.3$ presented in Schechter form by Fu et al. (2025) into the star formation rate function (SFRF). We perform this conversion by expressing the $H\alpha$ luminosity via SFR using two SFR— $L_{H\alpha}$ calibrations: the T19 calibration ($Z_* = Z_{\odot}$), and our new SFR($H\alpha$) calibration given in Eq. (2), which, by design, takes the dependence of the SFR— $L_{H\alpha}$ relation on metallicity into account. Following previous studies, we then integrate both SFRFs down to $\text{SFR} = 0.24 M_{\odot} \text{ yr}^{-1}$ which corresponds to $M_{UV} = -17$ (Bouwens et al. 2015). The resulting ρ_{SFR} decreases from $\approx 0.017 M_{\odot} \text{ yr}^{-1} \text{ Mpc}^{-3}$ to $\approx 0.015 M_{\odot} \text{ yr}^{-1} \text{ Mpc}^{-3}$, or by $\approx 12\%$, when using the new calibration. This suggests that the effect of the evolving SFR— $L_{H\alpha}$ relation on ρ_{SFR} is moderate, likely because galaxies in which the SFR bias is highest contribute little to ρ_{SFR} . For example, galaxies with $\text{SFR} < 10 M_{\odot} \text{ yr}^{-1}$ contribute less than 30% to the total ρ_{SFR} . If we integrate the SFRF only up to $\text{SFR} = 10 M_{\odot} \text{ yr}^{-1}$, the change in ρ_{SFR} would be more pronounced: ρ_{SFR} would decrease by $\approx 29\%$.

The SFR bias also affects the correlations between the SFR and other galaxy properties, such as stellar mass. In Fig. 4, we show the SFR— M_* relation, also known as the star formation main sequence (SFMS; Noeske et al. 2007), in the *JWST* All the Little Things (ALT) survey (Naidu et al. 2024; Di Cesare et al. 2025). We apply different SFR($H\alpha$) calibrations to the dust-corrected $H\alpha$ luminosities and calculate the slope of the SFMS. The slope increases by $\Delta \log \text{SFR} / \Delta \log M_* = 0.08 \pm 0.02$ ($20 \pm 6\%$) when we use Eq. (3) instead of the T19 calibration to calculate the SFRs. Equation (2) yields similar results, although they are less significant ($\Delta \log \text{SFR} / \Delta \log M_* = 0.02 \pm 0.03$). In addition, we find that the scatter in the SFMS decreases by $\Delta \sigma_{\text{SFR}} \approx 0.04$ dex ($\approx 14\%$) when using Eq. (3), most noticeably at the low-mass end ($\Delta \sigma_{\text{SFR}} \approx 0.06$ dex at $\log_{10}(M_*/M_{\odot}) < 7$). In contrast, Eq. (2) produces almost the same scatter as the T19 calibration ($\Delta \sigma_{\text{SFR}} \lesssim 0.01$ dex). We note that the SFMS in

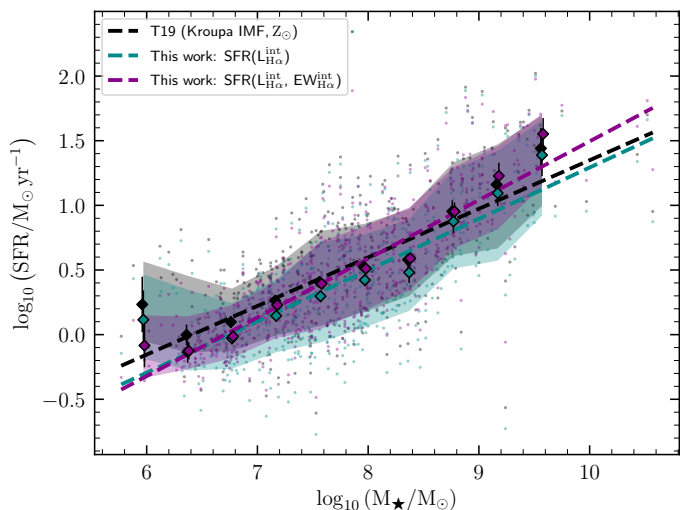


Fig. 4. Star formation main sequence (SFMS) in the *JWST* ALT survey (Naidu et al. 2024; Di Cesare et al. 2025) with SFRs calculated using the T19 calibration (gray) and the new SFR($H\alpha$) calibrations given in Eq. (2) (cyan) and Eq. (3) (magenta). The diamonds show the running median, with the error bars indicating the standard error on the median. The shaded regions indicate the 68% (1σ) confidence interval. The dashed lines show the linear regression fits to the SFMS individually for each calibration.

Fig. 4 is affected by selection effects: some low-mass galaxies are not detected in observations due to their faintness, resulting in a shallow SFMS slope. Temporary cessation or strong suppression of star formation in galaxies during so-called mini-quenching events (e.g., Gelli et al. 2023; Looser et al. 2025) can further amplify this bias. However, a comprehensive discussion of caveats associated with the SFMS slope measurements is beyond the scope of this paper (this discussion can be found in Di Cesare et al. 2025).

4.2. Dust attenuation

In Sect. 3, we ignored the effects of dust attenuation, assuming that the $H\alpha$ line measurements (i.e., $L_{H\alpha}$ and $EW_{H\alpha}$) can be corrected for these effects without errors. This assumption is also usually made for the SFR($H\alpha$) calibrations presented in the literature. However, dust attenuation is known to be an important source of systematic error in the $H\alpha$ -derived SFRs (e.g., Hopkins et al. 2001). This effect likely persists even at $z \gtrsim 4$ as the number of dust in $H\alpha$ -emitters at these redshifts is found to be non-negligible (e.g., Covelo-Paz et al. 2025 reported the median $A_{H\alpha} \approx 0.5$ mag for a sample of ≈ 1000 $H\alpha$ -emitters at $4 \lesssim z \lesssim 6$).

Here, we test the possibility of deriving SFRs directly from the observed $H\alpha$ emission without prior dust corrections. We use the dust-attenuated $H\alpha$ luminosity ($L_{H\alpha}^{\text{obs}}$) and equivalent width ($EW_{H\alpha}^{\text{obs}}$) from SPHINX, calculated as described in Sect. 2, and fit the same linear relations between the SFR, $L_{H\alpha}$, and $EW_{H\alpha}$ as in Sect. 3. We present the resulting SFR($H\alpha$) calibrations in Sect. B. The calibration that only depends on $L_{H\alpha}^{\text{obs}}$ (Eq. (B.1); Fig. 5, cyan) yields RMSE = 0.39 dex, while the calibration that additionally depends on $EW_{H\alpha}^{\text{obs}}$ (Eq. (B.2); Fig. 5, magenta) yields RMSE = 0.22 dex. In both cases, the RMSE is significantly higher than the RMSEs calculated using the calibrations that are based on the intrinsic $H\alpha$ properties (see Sect. 3). Moreover, the SFRs are significantly underestimated at high luminosities

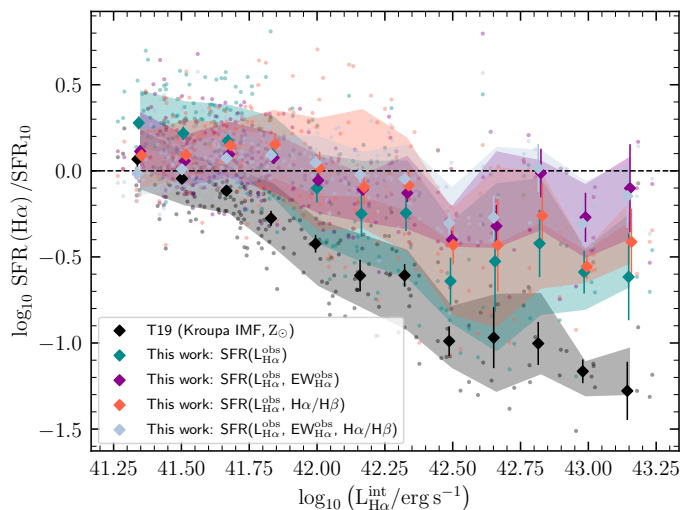


Fig. 5. Same as Fig. 3, but for the observed (i.e., dust-attenuated) $H\alpha$. In addition to $L_{H\alpha}$ and $EW_{H\alpha}$, two SFR($H\alpha$) calibrations use the Balmer decrement ($H\alpha/H\beta$) to predict the SFR (orange and light blue). The equations for the new calibrations are given in Sect. B.

ties ($\log_{10}(L_{H\alpha}^{\text{int}}/\text{erg s}^{-1}) \gtrsim 42.5$), with Eq. (B.1) and Eq. (B.2) producing the median $\Delta_{\text{SFR}} = -0.52$ and $\Delta_{\text{SFR}} = -0.27$, respectively. This can be explained by the fact that high- $L_{H\alpha}^{\text{int}}$ galaxies in SPHINX have very high attenuation values ($A_{H\alpha} \gtrsim 2$) on average, which we are unable to fully correct for while simultaneously trying to model the SFRs of low- $L_{H\alpha}^{\text{int}}$ galaxies. However, we caution that $A_{H\alpha}$ like this are not reported in high-redshift observations (see Sect. 2), and it might therefore still be possible in practice to make accurate SFR estimates based on the dust-attenuated $H\alpha$.

We also test whether the Balmer decrement ($L_{H\alpha}^{\text{obs}}/L_{H\beta}^{\text{obs}}$, hereafter $H\alpha/H\beta$), whose measurements are commonly used to calculate the dust corrections for $H\alpha$, can be a useful parameter to include in the SFR($H\alpha$) calibration. Interestingly, we find that the $H\alpha/H\beta$ -based calibration (Eq. (B.3); Fig. 5, orange) yields RMSE = 0.29 dex, which is ≈ 0.07 dex higher than the RMSE calculated using the $EW_{H\alpha}^{\text{obs}}$ -based calibration. This indicates that $H\alpha/H\beta$ is not as powerful as $EW_{H\alpha}^{\text{obs}}$ in constraining the SFRs of the SPHINX galaxies. This result is surprising because $H\alpha/H\beta$ is commonly regarded as a robust indicator of dust attenuation ($A_{H\alpha}$), while $EW_{H\alpha}^{\text{obs}}$ is in principle mostly independent of it. However, we still find a negative correlation between $EW_{H\alpha}^{\text{obs}}$ and $A_{H\alpha}$ in SPHINX ($r = -0.71$, $p < 10^{-6}$; Fig. 6), possibly because the amount of dust increases with the age of the stellar population, a parameter to which $EW_{H\alpha}^{\text{obs}}$ is sensitive. Further, unlike $H\alpha/H\beta$, $EW_{H\alpha}^{\text{obs}}$ correlates with stellar metallicity, allowing for an even more accurate prediction of the SFRs.

Inclusion of both $H\alpha/H\beta$ and $EW_{H\alpha}^{\text{obs}}$ in the calibration (Eq. (B.4); see also Fig. 5, light blue) provides the best performance among the considered models (RMSE = 0.16 dex). Observationally, however, the $H\alpha/H\beta$ measurements are hampered by slit losses and the requirement of a broader wavelength coverage. This implies that the benefits of including $H\alpha/H\beta$ in the SFR($H\alpha$) calibration are likely limited, with $EW_{H\alpha}^{\text{obs}}$ remaining a key addition to the calibration.

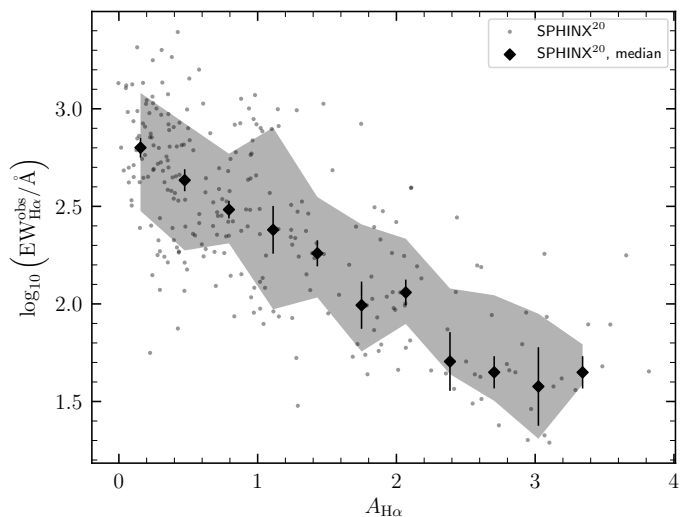


Fig. 6. $H\alpha$ equivalent width vs. dust attenuation in SPHINX. The diamonds show the running median, with the error bars indicating the standard error on the median. The shaded region indicates the 68% (1σ) confidence interval. We note that the $A_{H\alpha}$ values from SPHINX might be overestimated compared to the typical $A_{H\alpha}$ values measured in star-forming galaxies at $z \gtrsim 3$ (see Sect. 2).

4.3. Caveats

When using the $SFR(H\alpha)$ calibrations given in Eq. (2) and Eq. (3), it is important to take proper account of the scope of applicability of these calibrations and the assumptions made to derive them. In particular, the selection criteria described in Sect. 2 imply that the new calibrations can be applied to a flux-limited sample when the following conditions are met:

- $4 \lesssim z \lesssim 10$;
- $L_{H\alpha}^{obs} \gtrsim 10^{41} \text{ erg s}^{-1}$.

It is already possible to extend the calibrations to $L_{H\alpha}^{obs} < 10^{41} \text{ erg s}^{-1}$ with SPHINX, but a larger halo catalog than the currently available SPDRv1 catalog is needed to create a complete $H\alpha$ sample down to very low luminosities. At low redshifts ($z \lesssim 4$), the SFHs become less bursty and the metallicities increase, rendering the classical calibrations more suitable. Finally, at high redshift ($z \gtrsim 10$), it remains to be established whether the new calibrations can be used, as the physical conditions of star formation at these redshifts are poorly understood.

We also stress the fact that the new calibrations assume the BPASSv2.2 SPS model with a Kroupa-type IMF (see Sect. 2). Figure 1 shows that the choice of the IMF significantly affects the predicted SFRs, resulting in a systematic error of up to ≈ 0.2 dex (see also Jeřábková et al. 2018, who studied the effect of a non-universal IMF on the $SFR-L_{H\alpha}$ relation). The choice of the SPS model, in particular, whether the model includes binary stars, results in a smaller error (≈ 0.05 dex), possibly because binary stars have little effect on the LyC luminosity in the first ~ 3 Myrs of a stellar population when the bulk of ionizing photons is produced (e.g., Rosdahl et al. 2018), but this effect is still non-negligible. In the future, these systematic errors can be reduced by testing the SPS models and constraining the IMF at $z > 4$, for instance, by means of deep rest-frame UV spectroscopy (e.g., Steidel et al. 2016; Chisholm et al. 2019).

5. Summary

In this work, we study the relation between $H\alpha$ emission and the SFR in the SPHINX cosmological simulations at $4.64 \leq z \leq 10$. Using the simulated galaxy data from the SPHINX Public Data Release, Version 1 (Katz et al. 2023), we select a sample of star-forming galaxies that are representative of the $H\alpha$ -emitter population routinely observed with *JWST* at $z > 3$. The median $SFR-L_{H\alpha}$ relation in SPHINX exhibits a downturn at low luminosities (Fig. 1; $\log_{10}(L_{H\alpha}^{int}/\text{erg s}^{-1}) \sim 42.0-42.5$). This downturn is consistent with fainter galaxies having lower stellar metallicities ($Z_{\star} \sim 0.1Z_{\odot}$) and thus being more efficient producers of ionizing photons than brighter, relatively metal-enriched ($Z_{\star} \gtrsim 0.3Z_{\odot}$) galaxies. Furthermore, the $SFR-L_{H\alpha}$ relation exhibits a significant scatter at fixed luminosity, ranging from $\sigma_{SFR} \approx 0.04$ dex at $\log_{10}(L_{H\alpha}^{int}/\text{erg s}^{-1}) = 42.8$ to $\sigma_{SFR} \approx 0.17$ dex at $\log_{10}(L_{H\alpha}^{int}/\text{erg s}^{-1}) = 41.3$ (i.e., the scatter is larger at lower luminosities). We demonstrate that this scatter is primarily driven by the variations in the stellar metallicities and ages (Fig. 2), whereas other properties (e.g., M_{\star} and f_{esc}) play a less significant role.

Because of the metallicity dependence of the $SFR-L_{H\alpha}$ relation, the classical $SFR(H\alpha)$ calibrations (e.g., Kennicutt 1998; Eq. (1)) overestimate the SFRs of faint galaxies in SPHINX on average by $\Delta_{SFR} \equiv SFR(H\alpha)/SFR_{10} \gtrsim 0.1$ dex (Fig. 3, black). In Eq. (2), we propose a new $SFR(H\alpha)$ calibration that depends on the intrinsic $H\alpha$ luminosity alone and reduces the error in the predicted SFRs by $\Delta_{RMSE} \approx 0.04$ dex (Fig. 3, cyan). To address the scatter in the $SFR-L_{H\alpha}$ relation, we propose another $SFR(H\alpha)$ calibration in Eq. (3). This calibration additionally depends on the $H\alpha$ equivalent width, a parameter that is sensitive to the stellar metallicity and age (Fig. 2), and further improves the SFR estimate, reducing the error by a total of $\Delta_{RMSE} \approx 0.06$ dex (Fig. 3, magenta). The new $SFR(H\alpha)$ calibrations affect the galaxy population statistics at high redshift ($z \sim 6$): the inferred ρ_{SFR} decreases by $\approx 12\%$, and the slope of the SFMS increases by $\Delta \partial \log SFR / \partial \log M_{\star} = 0.08 \pm 0.02$ (Fig. 4).

Acknowledgements. We thank the anonymous referee for the insightful comments that helped improve the manuscript. We also thank Thibault Garel, Pascal Oesch, Irene Shivaei, Charlotte Simmonds, Andrew Hopkins, Daniel Schaerer, and Rashmi Gottumukkala for useful comments and productive discussions. We gratefully acknowledge support from the CBPsmn (PSMN, Pôle Scientifique de Modélisation Numérique) of the ENS de Lyon for the computing resources. Funded by the European Union (ERC, AGENTS, 101076224). Views and opinions expressed are however those of the author(s) only and do not necessarily reflect those of the European Union or the European Research Council. Neither the European Union nor the granting authority can be held responsible for them. This work made extensive use of several open-source software packages, and we gratefully acknowledge the efforts of their authors: NUMPY (Harris et al. 2020), ASTROPY (Astropy Collaboration et al. 2022), MATPLOTLIB (Hunter 2007), IPYTHON (Perez & Granger 2007), and SCIKIT-LEARN (Pedregosa et al. 2011).

References

- Asada, Y., Sawicki, M., Abraham, R., et al. 2024, *MNRAS*, 527, 11372
 Astropy Collaboration, Price-Whelan, A. M., Lim, P. L., et al. 2022, *ApJ*, 935, 167
 Behroozi, P., Wechsler, R. H., Hearin, A. P., & Conroy, C. 2019, *MNRAS*, 488, 3143
 Bezanson, R., Labbe, I., Whitaker, K. E., et al. 2024, *ApJ*, 974, 92
 Bouché, N., Dekel, A., Genzel, R., et al. 2010, *ApJ*, 718, 1001
 Bouwens, R. J., Illingworth, G. D., Oesch, P. A., et al. 2015, *ApJ*, 803, 34
 Carvajal-Bohorquez, C., Ciesla, L., Laporte, N., et al. 2025, *A&A*, 704, A290
 Chisholm, J., Rigby, J. R., Bayliss, M., et al. 2019, *ApJ*, 882, 182
 Chruślińska, M., Pakmor, R., Matthee, J., & Matsuno, T. 2024, *A&A*, 686, A186
 Clarke, L., Shapley, A. E., Sanders, R. L., et al. 2024, *ApJ*, 977, 133

- Cole, J. W., Papovich, C., Finkelstein, S. L., et al. 2025, *ApJ*, 979, 193
- Covelo-Paz, A., Giovinazzo, E., Oesch, P. A., et al. 2025, *A&A*, 694, A178
- Cullen, F., McLure, R. J., Dunlop, J. S., et al. 2019, *MNRAS*, 487, 2038
- Curti, M., Maiolino, R., Curtis-Lake, E., et al. 2024, *A&A*, 684, A75
- Davies, L. J. M., Lagos, C. d. P., Katsianis, A., et al. 2019, *MNRAS*, 483, 1881
- De Looze, I., Cormier, D., Leboutteiller, V., et al. 2014, *A&A*, 568, A62
- Di Cesare, C., Matthee, J., Naidu, R. P., et al. 2025, arXiv e-prints, arXiv:2510.19044
- Endsley, R., Stark, D. P., Whitler, L., et al. 2024, *MNRAS*, 533, 1111
- Ferland, G. J., Chatzikos, M., Guzmán, F., et al. 2017, *Rev. Mexicana Astron. Astrofis.*, 53, 385
- Fisher, R., Bowler, R. A. A., Stefanon, M., et al. 2025, *MNRAS*, 539, 109
- Flores Velázquez, J. A., Gurvich, A. B., Faucher-Giguère, C.-A., et al. 2021, *MNRAS*, 501, 4812
- Fu, S., Sun, F., Jiang, L., et al. 2025, *ApJ*, 987, 186
- Gelli, V., Salvadori, S., Ferrara, A., Pallottini, A., & Carniani, S. 2023, *ApJ*, 954, L11
- Götberg, Y., de Mink, S. E., & Groh, J. H. 2017, *A&A*, 608, A11
- Gunawardhana, M. L. P., Hopkins, A. M., Bland-Hawthorn, J., et al. 2013, *MNRAS*, 433, 2764
- Hao, C.-N., Kennicutt, R. C., Johnson, B. D., et al. 2011, *ApJ*, 741, 124
- Harris, C. R., Millman, K. J., van der Walt, S. J., et al. 2020, *Nature*, 585, 357
- Hayes, M., Schaerer, D., & Östlin, G. 2010, *A&A*, 509, L5
- Hopkins, A. M., Connolly, A. J., Haarsma, D. B., & Cram, L. E. 2001, *AJ*, 122, 288
- Hunter, J. D. 2007, *Computing in Science & Engineering*, 9, 90
- Iyer, K. G., Tacchella, S., Genel, S., et al. 2020, *MNRAS*, 498, 430
- Jeřábková, T., Zonoozi, A. H., Kroupa, P., et al. 2018, *A&A*, 620, A39
- Katz, H., Rosdahl, J., Kimm, T., et al. 2023, *The Open Journal of Astrophysics*, 6, 44
- Kennicutt, R. C. & Evans, N. J. 2012, *ARA&A*, 50, 531
- Kennicutt, Jr., R. C. 1998, *ARA&A*, 36, 189
- Kroupa, P. 2001, *MNRAS*, 322, 231
- Laursen, P., Sommer-Larsen, J., & Andersen, A. C. 2009, *ApJ*, 704, 1640
- Leitherer, C., Schaerer, D., Goldader, J. D., et al. 1999, *ApJS*, 123, 3
- Lilly, S. J., Carollo, C. M., Pipino, A., Renzini, A., & Peng, Y. 2013, *ApJ*, 772, 119
- Lin, X., Egami, E., Sun, F., et al. 2026, *ApJ*, 997, 207
- Looser, T. J., D'Eugenio, F., Maiolino, R., et al. 2025, *A&A*, 697, A88
- Ly, C., Malkan, M. A., Kashikawa, N., et al. 2007, *ApJ*, 657, 738
- Markov, V., Gallerani, S., Ferrara, A., et al. 2025, *Nature Astronomy*, 9, 458
- Mascia, S., Pentericci, L., Calabrò, A., et al. 2024, *A&A*, 685, A3
- Matthee, J., Feltre, A., Maseda, M., et al. 2022, *A&A*, 660, A10
- Matthee, J. & Schaye, J. 2019, *MNRAS*, 484, 915
- Meyer, R. A., Oesch, P. A., Giovinazzo, E., et al. 2024, *MNRAS*, 535, 1067
- Michel-Dansac, L., Blaizot, J., Garel, T., et al. 2020, *A&A*, 635, A154
- Nagaraj, G., Ciardullo, R., Bowman, W. P., Lawson, A., & Gronwall, C. 2023, *The Astrophysical Journal*, 943, 5
- Naidu, R. P., Matthee, J., Kramarenko, I., et al. 2024, arXiv e-prints, arXiv:2410.01874
- Noeske, K. G., Weiner, B. J., Faber, S. M., et al. 2007, *ApJ*, 660, L43
- Pedregosa, F., Varoquaux, G., Gramfort, A., et al. 2011, *Journal of Machine Learning Research*, 12, 2825
- Perez, F. & Granger, B. E. 2007, *Computing in Science and Engineering*, 9, 21
- Piric, C. A., Best, P. N., Duncan, K. J., et al. 2025, *MNRAS*, 541, 1348
- Rosdahl, J., Blaizot, J., Aubert, D., Stranex, T., & Teyssier, R. 2013, *MNRAS*, 436, 2188
- Rosdahl, J., Blaizot, J., Katz, H., et al. 2022, *MNRAS*, 515, 2386
- Rosdahl, J., Katz, H., Blaizot, J., et al. 2018, *MNRAS*, 479, 994
- Salpeter, E. E. 1955, *ApJ*, 121, 161
- Scholte, D., Cullen, F., Carnall, A. C., et al. 2025, *MNRAS*, 540, 1800
- Shim, H., Colbert, J., Teplitz, H., et al. 2009, *ApJ*, 696, 785
- Shivaei, I., Naidu, R. P., Rodríguez Montero, F., et al. 2025, arXiv e-prints, arXiv:2509.01795
- Sobral, D., Smail, I., Best, P. N., et al. 2013, *MNRAS*, 428, 1128
- Sparre, M., Hayward, C. C., Springel, V., et al. 2015, *MNRAS*, 447, 3548
- Stanway, E. R. & Eldridge, J. J. 2018, *MNRAS*, 479, 75
- Steidel, C. C., Strom, A. L., Pettini, M., et al. 2016, *ApJ*, 826, 159
- Sun, F., Wang, F., Yang, J., et al. 2025, *ApJ*, 980, 12
- Tacchella, S., Forbes, J. C., & Caplar, N. 2020, *MNRAS*, 497, 698
- Teyssier, R. 2002, *A&A*, 385, 337
- Theios, R. L., Steidel, C. C., Strom, A. L., et al. 2019, *ApJ*, 871, 128
- Wan, J. T., Tacchella, S., D'Eugenio, F., Johnson, B. D., & van der Wel, A. 2025, *MNRAS*, 539, 2891
- Wang, E. & Lilly, S. J. 2020, *ApJ*, 892, 87
- Weibel, A., Oesch, P. A., Barrufet, L., et al. 2024, *MNRAS*, 533, 1808
- Wilkins, S. M., Lovell, C. C., & Stanway, E. R. 2019, *MNRAS*, 490, 5359
- Zavala, J. A., Casey, C. M., Manning, S. M., et al. 2021, *ApJ*, 909, 165

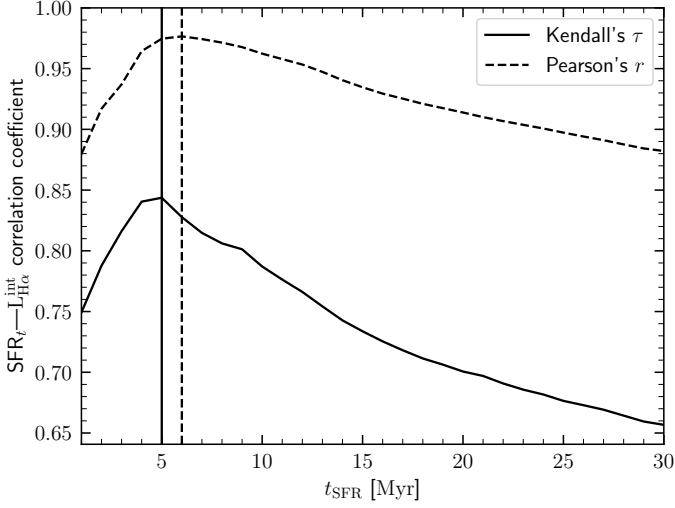


Fig. A.1. Correlation coefficients between the SFR and $L_{\text{H}\alpha}^{\text{int}}$ as a function of the star formation timescale, t_{SFR} .

Appendix A: Timescales of star formation traced by H α

It is commonly assumed in the literature that H α traces star formation over the last $t_{\text{SFR}} = 10$ Myr. To test this, we use the SFHs published as part of SPDRv1 and calculate the average of the SFR over the last $t_{\text{SFR}} = 1, 2, \dots, 30$ Myr. We then calculate the correlation coefficients between $L_{\text{H}\alpha}^{\text{int}}$ and the SFRs averaged over different timescales. We find that Pearson's r is highest between $4 \text{ Myr} \lesssim t \lesssim 12 \text{ Myr}$ ($r > 0.95$), with a maximum at $t_{\text{SFR}} = 6$ Myr ($r = 0.98$; Fig. A.1, dashed line). Similarly, Kendall's τ peaks at $t_{\text{SFR}} = 5$ Myr ($\tau = 0.84$; Fig. A.1, solid line). This suggests that a slightly shorter timescale ($t_{\text{SFR}} = 5\text{--}6$ Myr) might be more appropriate for H α . Nevertheless, for consistency with previous works, we use the SFRs averaged over $t_{\text{SFR}} = 10$ Myr throughout this paper.

Appendix B: SFR(H α) calibrations for the dust-attenuated H α line measurements

$$\begin{aligned} \log_{10} \left[\frac{\text{SFR}}{M_{\odot} \text{ yr}^{-1}} \right] &= \log_{10} \left[\frac{L_{\text{H}\alpha}^{\text{obs}}}{\text{erg s}^{-1}} \right] - 41.00 \\ &+ 0.66 \left(\log_{10} \left[\frac{L_{\text{H}\alpha}^{\text{obs}}}{\text{erg s}^{-1}} \right] - 41.46 \right) \end{aligned} \quad (\text{B.1})$$

$$\begin{aligned} \log_{10} \left[\frac{\text{SFR}}{M_{\odot} \text{ yr}^{-1}} \right] &= \log_{10} \left[\frac{L_{\text{H}\alpha}^{\text{obs}}}{\text{erg s}^{-1}} \right] - 41.00 \\ &+ 0.23 \left(\log_{10} \left[\frac{L_{\text{H}\alpha}^{\text{obs}}}{\text{erg s}^{-1}} \right] - 41.46 \right) \\ &- 0.67 \left(\log_{10} \left[\frac{\text{EW}_{\text{H}\alpha}^{\text{obs}}}{\text{\AA}} \right] - 2.41 \right) \end{aligned} \quad (\text{B.2})$$

$$\begin{aligned} \log_{10} \left[\frac{\text{SFR}}{M_{\odot} \text{ yr}^{-1}} \right] &= \log_{10} \left[\frac{L_{\text{H}\alpha}^{\text{obs}}}{\text{erg s}^{-1}} \right] - 41.00 \\ &+ 0.58 \left(\log_{10} \left[\frac{L_{\text{H}\alpha}^{\text{obs}}}{\text{erg s}^{-1}} \right] - 41.46 \right) \\ &+ 5.81 \left(\log_{10} \left(L_{\text{H}\alpha}^{\text{obs}} / L_{\text{H}\beta}^{\text{obs}} \right) - 0.51 \right) \end{aligned} \quad (\text{B.3})$$

$$\begin{aligned} \log_{10} \left[\frac{\text{SFR}}{M_{\odot} \text{ yr}^{-1}} \right] &= \log_{10} \left[\frac{L_{\text{H}\alpha}^{\text{obs}}}{\text{erg s}^{-1}} \right] - 41.00 \\ &+ 0.22 \left(\log_{10} \left[\frac{L_{\text{H}\alpha}^{\text{obs}}}{\text{erg s}^{-1}} \right] - 41.46 \right) \\ &- 0.59 \left(\log_{10} \left[\frac{\text{EW}_{\text{H}\alpha}^{\text{obs}}}{\text{\AA}} \right] - 2.41 \right) \\ &+ 3.74 \left(\log_{10} \left(L_{\text{H}\alpha}^{\text{obs}} / L_{\text{H}\beta}^{\text{obs}} \right) - 0.51 \right) \end{aligned} \quad (\text{B.4})$$